On the differences in trimethylaluminum infiltration into PMMA and PLA polymers for sequential infiltration synthesis: insights from experiment and first principles simulations

Michele Perego[1,], Alessia Motta[1,2 §], Karl Rönnby[3 §], Forest Tung Jie Yap[3], Gabriele Seguini[1], Claudia Wiemer[1], Michael Nolan[3,*]*

[1] CNR-IMM, Unit of Agrate Brianza, Via C. Olivetti 2, I-20864 Agrate Brianza, Italy

[2] Politecnico di Milano, Dipartimento di Energia, Via Ponzio 34/3, 20133 Milano, Italy

[3] Tyndall National Institute, Lee Maltings, University College Cork, T12R5CP, Ireland

[*] Corresponding authors: michele.perego@cnr.it , michael.nolan@tyndall.ie

[§] these authors contributed equally

Abstract

Sequential infiltration synthesis (SIS) is a powerful approach for templated growth of solid materials such as oxides or metals that exploits the difference in interaction of a precursor molecule with a polymer or block copolymer. While there have been studies showing that infiltration of trimethyl-alumina (TMA) in polymers can be used to grow Al_2O_3 there are still many atomic level details of the SIS process that require more investigation, including the origin of the differences in infiltration of TMA into different polymers. In this paper, we investigated in detail the Infiltration of Al_2O_3 into poly (methyl methacrylate) (PMMA) and poly (lactic acid) (PLA) experimentally and theoretically. SIS was performed in a standard ALD reactor, operating at 70°C in quasi-static mode, using TMA and water as the metal and oxygen precursors, respectively. *Operando* spectroscopic ellipsometry

and *ex-situ* x-ray photoelectron spectroscopy (XPS) evidenced that Al_2O_3 incorporation in PLA is significantly higher than in PMMA even if, in both cases, TMA incorporation occurs through the formation of an Al-O covalent bond at the C-O-C group. The extent of swelling of the polymers upon TMA infiltration is assessed and is clearly larger for TMA in PLA than in PMMA. First principles density functional theory (DFT) calculations highlighted that both polymers display swelling upon TMA infiltration, saturating with increasing TMA, consistent with *operando* ellipsometry observations. The DFT results also show the origin of the larger swelling in PLA compared to TMA. Changes in vibrational modes of carbonyl backbone groups in the polymers are used to demonstrate TMA-polymer interactions from both experiment and simulation. The differences in TMA infiltration and swelling arises from differences in the TMA-polymer C-O-C group interaction, which is more exothermic in PLA than in PMMA, in agreement with experimental results. The combination of experimental and theoretical studies herein reported provides a toolkit to disclose the complexities of SIS at the molecular level.

Introduction

Sequential infiltration synthesis (SIS) is a vapor phase infiltration (VPI) technique to produce organic-inorganic hybrid materials and/or inorganic nanostructures through infiltration of an inorganic precursor into a suitable polymer template.[1–5] SIS uses the same approach as atomic layer deposition (ALD) through introducing precursors/co-reactants in separate, sequential steps and exploiting self-limiting precursor reaction chemistry to deposit target materials.[6] Despite the broad interest in and importance of SIS for semiconductor nanolithography,[7–9] nanopatterning,[10–12] organic electronics[13–15] and water membrane technology,[16–19] the number of inorganic materials that can be grown by SIS remains quite limited.[20–23] To expand the library of materials that can be synthetized using this technique, widening its application fields and appeal, experimental and theoretical studies on the kinetics of sorption, diffusion and reaction mechanisms of precursors with the different polymer matrices are necessary. In this respect, the understanding of the fundamental physico-chemical mechanisms governing the infiltration of SIS precursors and co-reactants into the polymer matrix is very important to help with developing modelling tools for SIS, similar to the state of modelling of ALD,[24,25] with predictive capabilities, that will support the community in the search for novel precursors and the establishment of proper infiltration protocols.

Infiltration of Al_2O_3 into poly (methyl methacrylate) (PMMA) thin films using trimethyl aluminium (TMA) and H_2O as precursors has been widely investigated and is commonly considered as a reference system in the scientific community. Variation of sorption, diffusion and reaction of TMA into this specific polymer as a function of processing parameters have been well studied.[26–30] In particular, upon increasing the processing temperature, a progressive enhancement of TMA diffusivity is determined, but a concomitant reduction of TMA solubility and reactivity is induced, significantly decreasing the amount of TMA trapped into the polymer matrix. As a consequence, the effective incorporation of Al_2O_3 into the PMMA matrix is generally limited, irrespective of the processing temperature. Recent results have highlighted that several polymers, like poly(ethylene

terephthalate glycol) (PET-G),[31] polycaprolactone (PCL),[32] poly (lactic acid) (PLA) and poly(butylene succinate) (PBS) exhibit significantly higher reactivity to TMA compared to PMMA [33]. In particular, by monitoring the evolution of the film thickness during the infiltration process, *Petit et al.* demonstrated extremely efficient infiltration of Al_2O_3 into PET-G arising from the irreversible reaction of TMA with the polymer matrix which limits the out-diffusion of TMA.[31] Biswas *et al.* studied infiltration of Al_2O_3 into PMMA and PLC, demonstrating that the interaction of PCL with metal precursors is very strong, even though its ester functional groups are seemingly similar to those present in the more weakly interacting PMMA polymer.[32] Similarly, Padbury *et al.* reported that nearly 100% of the reactive groups in the PLC matrix react with TMA molecules, leading to a significant amount of Al_2O_3 incorporated into the polymer matrix during a single SIS cycle.[34] Finally, Motta *et al.* reported homogeneous growth of Al_2O_3 throughout the entire thickness of a 30 µm thick PBS freestanding membrane.[33] Moreover, Al_2O_3 mass uptake in PBS thin films was demonstrated to be much higher than in standard PMMA films, under the same process conditions. Consequently, having the same functional groups does not guarantee strong infiltration of the inorganic phase into the polymer matrix[35,36] but more understanding of the details of precursor infiltration is required.

Overall, data in the literature suggest that the limited reactivity of TMA with the PMMA matrix is more the exception than the rule. Interestingly, all these polymers are characterized by the presence of ester groups along the main polymer chain that are expected to act as reactive sites for TMA during the SIS process, but the work discussed above demonstrates that the presence of ester groups alone in the polymer is not sufficient to drive the SIS chemistry and other factors will also be important. Accordingly, the different position of the reactive sites along the polymer chains appears to play a crucial role, resulting in a clear variation of Al_2O_3 incorporation into the different polymer matrices.[31–34,37] More information about the reaction of TMA with these functional groups is necessary to better understand polymer–precursor interactions and investigate the fundamental mechanisms governing inorganic phase growth into a polymer matrix during the SIS process, but this

is challenging to elucidate with only experimental techniques and first principles simulations can contribute significantly to growing our understanding of SIS chemistries.

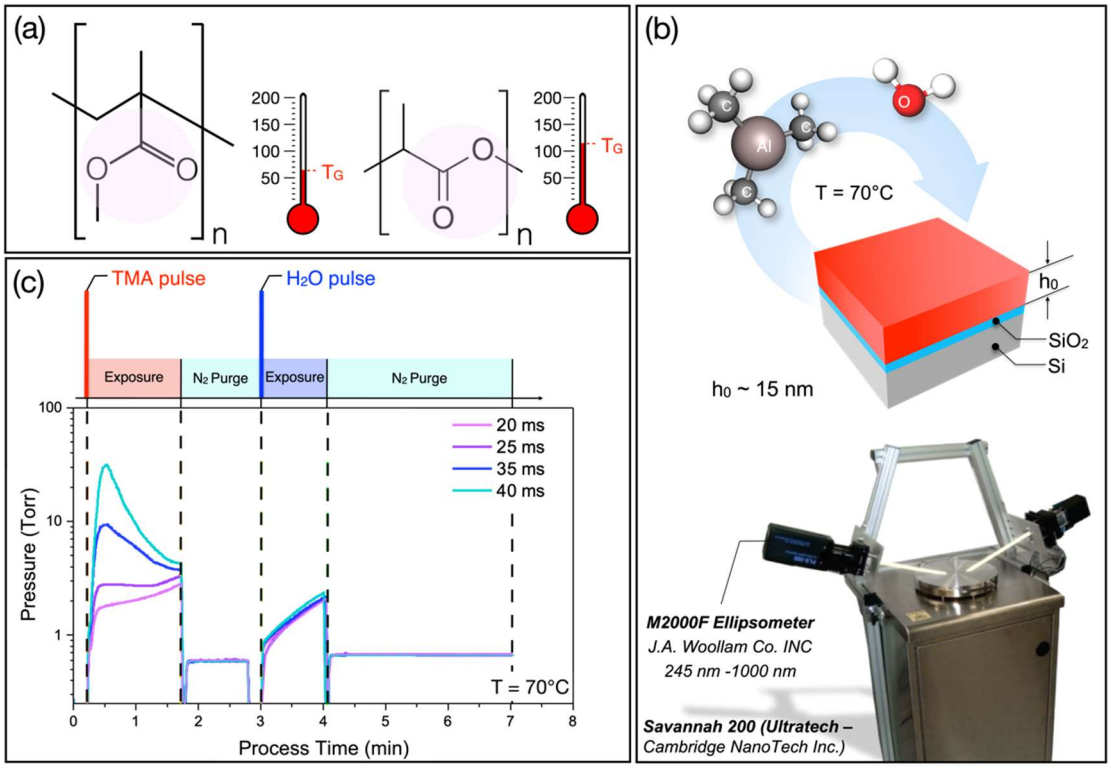

Figure 1: *(a) chemical structure of PMMA and PLA molecules with the indication of their glass transition temperatures. The pink shadows highlight the position of the ester groups in the two molecules. (b) Scheme of the experimental set-up showing the ALD reactor equipped with the in situ ellipsometer and the structure of the infiltrated samples. (c) Scheme of the typical SIS cycle along with the pressure evolution in the growth chamber for processes characterized by different durations of the TMA pulse. The duration of the H_2O pulse was kept fixed (t =15 ms) in all the processes.*

In this work, the infiltration of Al_2O_3 into PMMA and PLA thin films was investigated experimentally and, for the first time, theoretically with first principles density functional theory (DFT) simulations using both non-periodic and periodic models of the TMA-polymer interactions. The chemical structure of the two polymers is reported in **Figure 1a** together with the corresponding glass transition temperatures. Infiltration processes were performed in a conventional ALD reactor, operating in quasi-static mode at 70°C, using TMA and H_2O as metal and oxygen precursor, respectively, as shown in **Figure 1b**. Information about solubility and reactivity of TMA molecules in the two polymer matrices was obtained by monitoring polymer swelling by *operando* spectroscopic

ellipsometry (SE) and analysing chemical composition of the infiltrated polymers by *ex-situ* x-ray photoelectron spectroscopy (XPS). Experimental results were combined with DFT simulations of explicit TMA infiltration and polymer swelling to provide a consistent picture of TMA interaction with the different polymer matrices, identifying the energetically favourable binding configurations of TMA with PMMA and PLA polymer chains and elucidating the origin of the differences between the two polymers. In addition, we demonstrate that polymer swelling can be well described, and hence predicted, within DFT simulations which opens up new avenues to predicting novel precursor-polymer systems for SIS applications.

Methods

Sample preparation: 1 x 1 cm^2 Si samples were cut from a n-type (100) Si wafer. Si substrates were cleaned with 2-propanol and acetone in an ultrasonic bath and subsequently dried using a stream of ultrapure N_2. A 30 µm thick free-standing PLA film was supplied by Corapack®. PLA was dissolved in chloroform and spin coated on the1 x 1 cm^2 Si samples forming ~15 nm thick polymer films. PMMA (M_n = 15 kg mol^{-1}, PDI = 1.09) was acquired from Polymer Source. Inc. and dissolved in toluene. Then ~15 nm thick PMMA films were prepared by spin coating the PMMA solution on the 1 x 1 cm^2 Si samples. Before infiltration, the PMMA films were annealed at 200 °C for 300 s on a hot plate to remove residual toluene. A simplified scheme depicting the final structure of the samples is shown in **Figure 1b**.

Sequential Infiltration Synthesis process: SIS processes were performed at 70°C in a commercial cross-flow ALD reactor (Savannah S200, Ultratech Cambridge NanoTech) utilizing TMA and H_2O as organometallic and oxygen precursors, respectively. Before starting the process, the samples were kept at 70 °C for 30 minutes under N_2 flow (100 sccm, 0.66 Torr) to guarantee proper thermalization of the growth chamber. The SIS cycle comprised the following steps: TMA pulse, TMA exposure, TMA purge, H_2O pulse, H_2O exposure and H_2O purge. The duration (t_{TMA}) of

the TMA pulses was varied from 25 to 40 ms, while the duration of the H_2O pulse was 15 ms. The chamber was kept in static vacuum during the 90 s long TMA and 60 s long H_2O exposure steps by closing inlet and outlet valves. TMA purge time was 60 s. H_2O purge time was 180 s to guarantee complete removal of reaction by-products. A scheme of the SIS cycle and of the pressure evolution into the ALD reactor is reported in **Figure 1c**. A change of the t_{TMA} value determines a variation of the chamber pressure, consistently with the idea of a modification of TMA partial pressure in the growth chamber. After the SIS process, the samples were exposed to O_2 plasma (40 W, 10 min) to remove the polymer, resulting in the formation of Al_2O_3 films on the Si substrate.

Spectroscopic Ellipsometry: SE data were collected using a M-2000F (J. A. Woollam Co. Inc.) rotating compensator ellipsometer equipped with an Xe lamp. To enable *operando* measurements, the ALD reactor was equipped with a modified lid with two quartz windows that allow the incident light to reach the sample and the reflected light to be detected at a 70° angle with respect to the normal of the substrate plane. The assembly of the spectroscopic ellipsometer on top of the ALD reactor is shown in **Figure 1b**. *Ex-situ* SE measurements were performed at a fixed 75° incidence angle. The SE data were collected across a wavelength range spanning from 250 to 1000 nm with an acquisition time of 1.6 s. The data were analysed using version 2.3 of the EASE software package (J.A. Woollam Co. Inc). The thickness and refractive index of the polymer films during and after the SIS process were determined using a film stack model composed by a polymer layer on top of the thin SiO_2 film naturally formed on the surface of the Si substrate. A Cauchy layer model was used for the polymer layer. For each sample, the thickness of the native SiO_2 layer on top of the Si substrate was measured before spin casting and kept fixed during the analysis of the SE data following a procedure that is described in details in previous publications.[27–29]

X-ray Photoemission Spectroscopy: XPS measurements were performed using a PHI 5600 instrument equipped with a monochromatic Al Kα x-ray source (1486.6 eV) and a concentric hemispherical analyser. The spectra were collected at a take-off angle of 45°. Low resolution spectra

were acquired with a pass energy of 93.9 eV. High resolution spectra were acquired with a pass energy of 11.75 eV. Calibration of the spectrometer was accomplished using polycrystalline gold, silver, and copper samples. The binding energies of the Au $4f_{7/2}$, the Ag $3d_{5/2}$, and the Cu $2p_{3/2}$ core lines were determined to be 84.0 eV, 368.3 eV, and 932.7 eV, respectively. The analysis of the XPS spectra was performed using the Winspec software. To correct the energy shift induced by charging of the polymer films during the XPS measurements, the C 1*s* core level originated by the carbonyl group was used. The binding energy of this C *1s* signal was set to 289 eV.[38–40] The high resolution spectra were fitted using Shirley background and Voight functions to identify the different core level signals.

Density Functional Theory Simulations: Two model systems using DFT simulations were preformed to model complementary aspects of TMA infiltration in PLA and PMMA. The first model, similar to that previously used for RuO_4 infiltration in polystyrene and PMMA,[41] is a non-periodic, gas phase model that uses an oligomer of ten monomers for each polymer, and standard DFT relaxations. The non-periodic DFT calculations were performed with the TURBOMOLE software using the PBE0 hybrid exchange-correlation functional with a split valence, def-SV(P), basis set, which provides reliable results for similar calculations.[42–44] The self-consistent field (SCF) convergence criteria was 10^{-6} Ha and the structures were relaxed until an energy convergence of 10^{-3} Ha. IR vibrational modes were calculated using analytical force constants within the harmonic oscillator approximation.

The second model we use is a periodic supercell of the polymer that is periodic along the polymer chain, using a supercell with two explicit eight monomer chains of each polymer. This allows us to explore the impact of TMA content in the polymer, in particular the swelling of the two polymers, facilitating for the first time a direct comparison with the experimental results and also allows us to assess limitations associated with a non-periodic oligomer model of the polymer. Two further periodic models are used: the large model is used for infiltration and swelling described above and a smaller model of one chain that is six monomers long for the calculation of the IR vibrational

modes upon TMA infiltration and adduct formation (due to the high cost of these calculations). The periodic DFT calculations were carried out using the Vienna Ab initio Simulation Package (VASP) 5.4.[45–47] The Perdew-Burke-Ernzerhof (PBE) generalized gradient approximation of the exchange-correlation functional was used.[48] An 800 eV plane-wave cutoff energy was used which minimizes the Pulay stresses during ion and lattice relaxations. Projector augmented wave (PAW) potentials were used, with 1 valence electron for hydrogen, 4 for carbon, 6 for oxygen and 3 for aluminium.[49] Gaussian smearing with a width of 0.1 eV was used for all calculations. Grimme's version 3 dispersion correction was included to improve the description of non-covalent interactions between the polymer chains.[50] Structural relaxions used an electronic convergence criteria of 10^{-4} eV for each ionic step and a force convergence of 0.02 eV/Å. Phonon vibration modes were calculated using finite central difference with a displacement of 0.015 Å, using an electronic convergence criteria of 10^{-6} eV.

Experimental Results

Spectroscopic ellipsometry. *Operando* SE measurements allow the real time monitoring of the thickness evolution of the polymer matrix during the different steps of the SIS process.[27,51] Accordingly, the swelling ε(t) of the polymer template during the SIS process can be determined using the following equation:

$$\varepsilon(t) = \frac{h(t) - h_0}{h_0} \quad (1)$$

where *h(t)* indicates the thickness of the PMMA film at process time *t* and h_0 the thickness of the PMMA film at the beginning of the process, *i.e.* at process time $t = 0$. The swelling evolution as a function of time for the 15 nm thick PLA and PMMA films during a single SIS cycle at $T = 70$°C is reported in **Figure 2a** and **2b** respectively. The vertical black dashed lines mark the boundaries among the different step of the SIS process. For each polymer matrix, different swelling curves were

obtained by changing the duration (t_{TMA}) of the TMA pulse from 20 to 40 ms. All the samples exhibit similar swelling curves characterized by a fast swelling during the initial stages of the TMA exposure step followed by a level-off to a maximum swelling value (ε_{MAX}). This evolution is consistent with the idea that TMA molecules uniformly permeate the 15 nm thick polymer layers achieving a saturation condition with a concentration of TMA into the polymer matrix that depends on the solubility of TMA into the specific polymer under investigation.

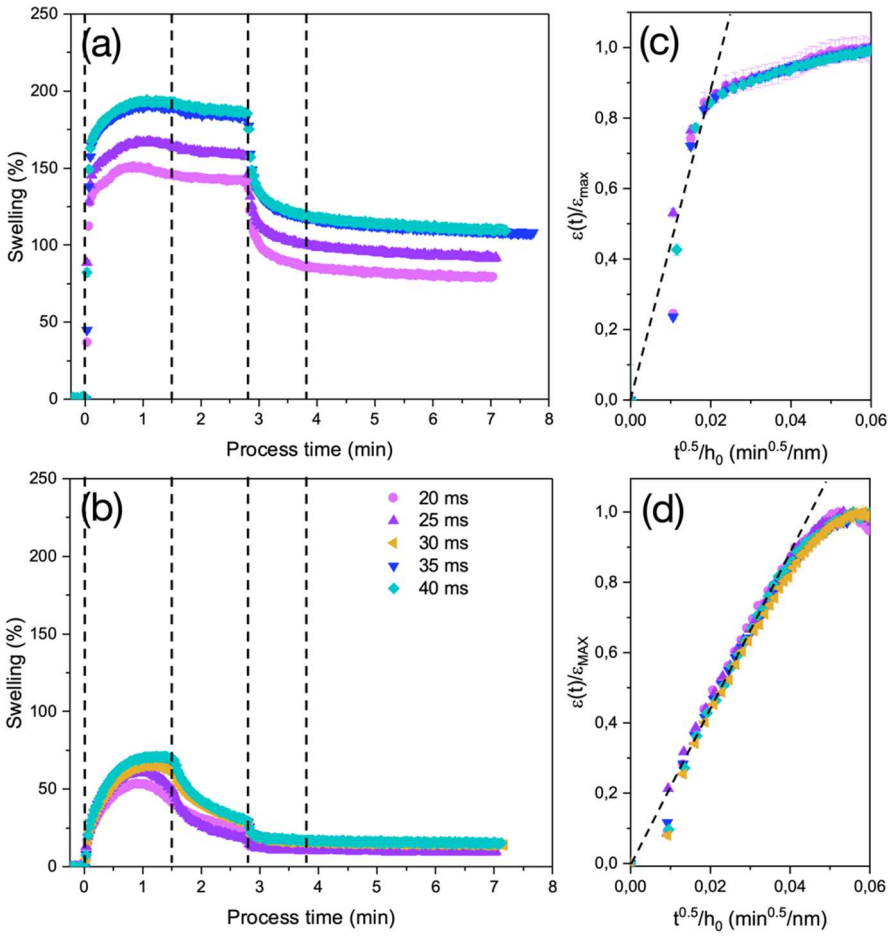

***Figure 2**: Swelling evolution as a function of time s for 15 nm thick PLA (a) and PMMA (b) thin films deposited on silicon substrates during the different steps of the sequential infiltration process. Black dashed lines mark the boundaries among the different steps of the process. The different curves correspond to different durations of the TMA pulse that is performed to inject the metal precursor into the growth chamber. Normalized swelling evolution as a function of $t^{1/2}/h_0$ for 15 nm thick PLA (c) and PMMA (d) thin films. The black dashed lines correspond to the fitting of the experimental data with equation (2).*

Interestingly, the swelling of the PLA matrix is much faster than that of PMMA with a much steeper swelling variation during the initial stages of the TMA exposure step, indicating that

diffusivity of TMA is higher in PLA than in PMMA. This is clearly highlighted in **figure 2c** and **2d** showing the evolution of the normalized swelling $\varepsilon(t)/\varepsilon_{MAX}$ as a function of $t^{1/2}/h_0$ for PLA and PMMA thin films, respectively. Previous studies[27,28,51] demonstrated that TMA diffusion into PMMA is governed by Fickian diffusion during the initial stages of the TMA exposure step, with a progressive increase of the $\varepsilon(t)/\varepsilon_{max}$ that is perfectly described by the following equation:

$$\varepsilon(t)/\varepsilon_{\max} \sim 4\sqrt{D/\pi}\, t^{1/2}/h_0 \qquad (2)$$

In this Fickian diffusion regime, the diffusion coefficient is simply determined as the slope of the linear fit (black dashed lines) of the $\varepsilon(t)/\varepsilon_{max}$ curves as a function of $t^{1/2}/h_0$ using **equation (2)**. In this way, the diffusion coefficient of TMA in PMMA at 70°C is determined to be 1.8 ± 0.1 x 10^{-14} cm^2/s, in perfect agreement with previous results in the literature.[27,28,51] In the case of PLA the fitting of the $\varepsilon(t)/\varepsilon_{\max}$ curves with equation (2) is somehow questionable because the polymer films exhibit a complex swelling evolution. Nevertheless, the fitting of the initial stages of the swelling returns a rough indication of the effective diffusivity of TMA in PLA that is found to be ~ 4.9 ± 0.3 x 10^{-13} cm^2/s.

According to Henry's law, higher the TMA partial pressure in the growth chamber, higher the TMA concentration in the polymer matrix and consequently larger its swelling. In this respect, both polymers exhibit a similar trend: a progressive increase of ε_{MAX} was induced when increasing t_{TMA} from 20 to 35 ms, while no further ε_{MAX} increase was observed for t_{TMA}= 40 ms, as shown in **Figure 3a** and **3b** for PLA and PMMA, respectively. This result suggests that the solubility limits of TMA into these polymer templates was achieved. It is worth noting that the ε_{MAX} values in the case of the PLA samples are significantly larger than the ones obtained in the case of the PMMA samples consistently with the idea that a larger amount of TMA has been incorporated into the PLA samples.

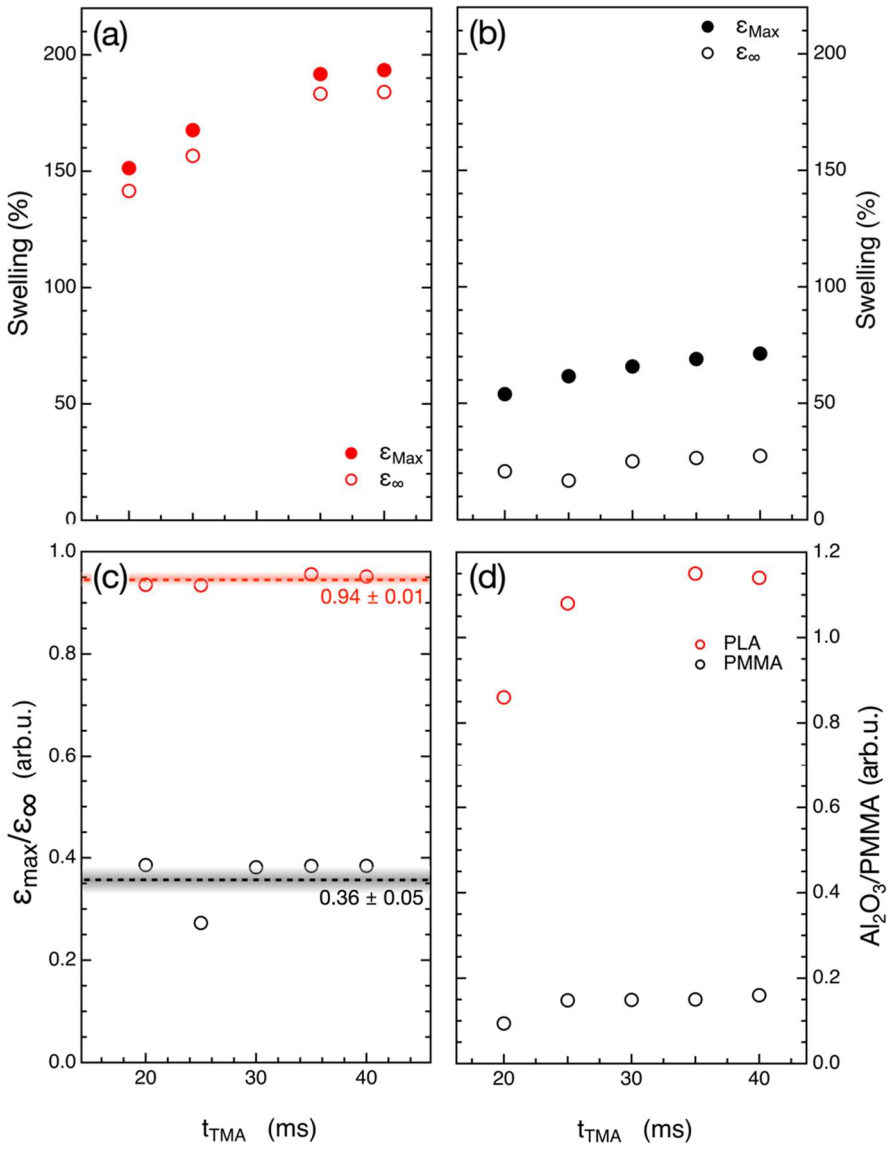

Figure 3: *ε_{MAX} (closed symbol) and ε_{∞} (open symbol) for PLA (a) and PMMA (b) reported as a function of TMA exposure time. (c) The ratio $\varepsilon_{\infty}/\varepsilon_{MAX}$ is reported as a function of TMA exposure time for PLA (red open symbols) and PMMA (black open symbols), respectively. Dashed lines correspond to the average $\varepsilon_{\infty}/\varepsilon_{MAX}$ values for PLA (red) and PMMA (black). (d) Thicknesses of the residual Al_2O_3 films upon removal of the PLA(red open symbols) and PMMA(black open symbols) matrices by O_2 plasma reported as a function of TMA exposure time.*

During TMA purging step the two polymer matrices exhibit significantly different behaviour. In particular, PMMA films are characterized by a fast and massive deswelling, fully consistent with previous results in the literature.[27,31] Conversely, almost no deswelling is observed in the PLA films. Polymer deswelling during the TMA purging step is associated with the desorption of TMA molecules which were not incorporated into the polymer matrix by a strong interaction with the

reactive sites of the polymer matrix. Information about the fraction of TMA molecules chemically trapped into the polymer matrix is obtained by fitting the deswelling curve with an exponential decay function:

$$\varepsilon(t) = \varepsilon_{\infty} + e^{-t/\tau} \quad (3)$$

where ε_{∞} corresponds to the film thickness at an infinite purging time and τ indicates the characteristic time of the deswelling process. The ε_{∞} values as a function of t_{TMA} are reported in **Figure 3a** and **3b** for PLA and PMMA, respectively. As highlighted in a very recent paper [28], the ratio $\varepsilon_{\infty}/\varepsilon_{MAX}$ indicates the fraction of TMA molecules that are stably incorporated into the polymer matrix through a chemical reaction. Interestingly, the ratio $\varepsilon_{\infty}/\varepsilon_{MAX}$ is fairly constant (**figure 3c**) for both polymers, with average values corresponding to 0.94 ± 0.01 for PLA and 0.36 ± 0.05 for PMMA. These results indicate that almost all the TMA molecules are adsorbed and chemically trapped into the PLA matrix. Conversely, PMMA exhibits a low TMA incorporation efficiency because of reduced sorption and weaker reactivity with TMA compared to PLA, even if the process is performed at a temperature that is identified to correspond to the thermodynamic equilibrium for the reaction of TMA molecules with the reactive sites of the PMMA matrix.[26]

Further confirmation of this interpretation of the SE data is provided by measuring the thickness of the residual Al_2O_3 film that is left over the Si substrate upon removal of the polymer template by a prolonged O_2 plasma treatment. The thicknesses of the Al_2O_3 films upon removal of the PLA and PMMA matrices are reported in **Figure 3d** as a function of t_{TMA}. The Al_2O_3 thickness values are normalized over the initial thickness h_0 of the polymer films. The normalized thickness values are fairly constant, within the experimental error, for PMMA, irrespective of the t_{TMA}. In the case of the PLA template, the normalized thickness values of the residual Al_2O_3 films progressively increases when increasing t_{TMA} and achieves a sort of saturation value for $t_{TMA} \geq 35$ ms. Additionally, the normalized thickness values of the residual Al_2O_3 films upon the removal of the PLA are determined

to be around one order of magnitude higher than those obtained using PMMA as a template, confirming that the amount of TMA stably incorporated in the PLA films is significantly larger than in the PMMA films, in good agreement with *operando* SE results.

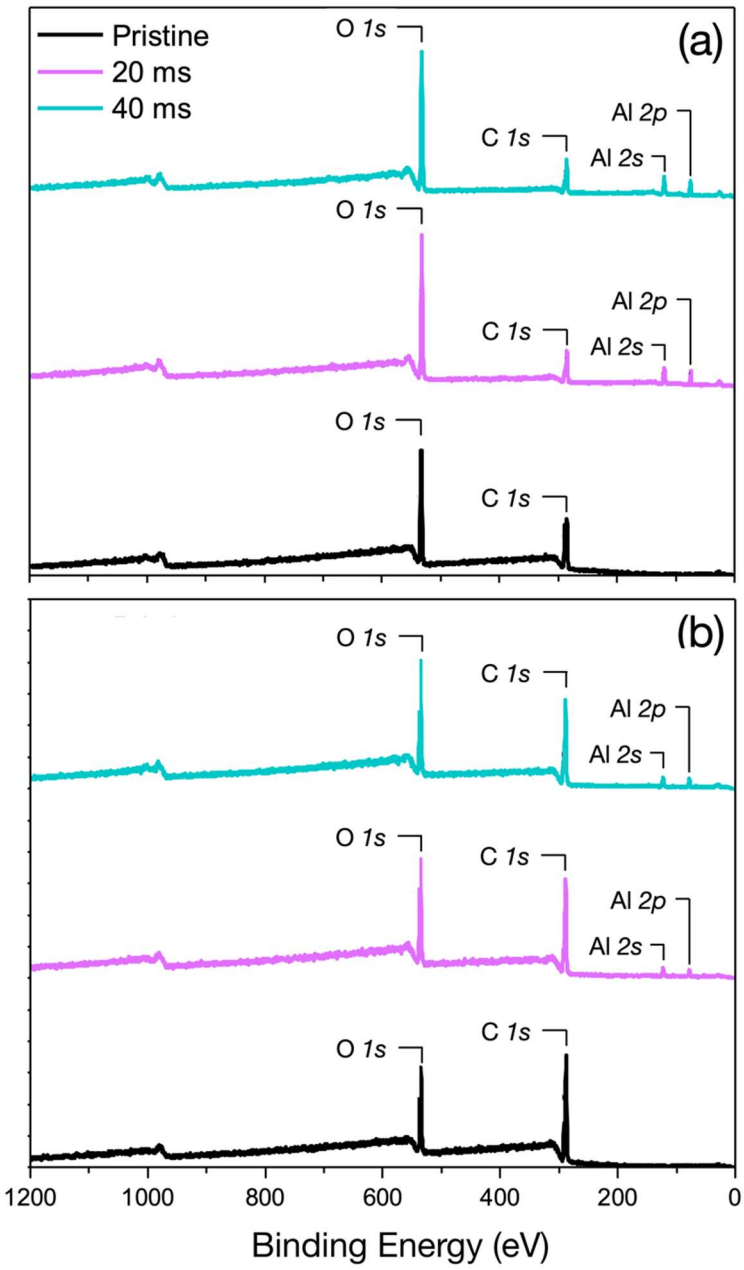

Figure 4: *low resolution XPS spectra of pristine and infiltrated 15 nm thick PLA (a) and PMMA (b) films. Main core level peaks are identified for each spectrum.*

X-ray Photoelectron Spectroscopy. As previously discussed, the almost negligible deswelling observed in the case of the PLA films during the TMA purging step points to stable incorporation of TMA molecules into the polymer template, resulting in efficient Al_2O_3 infiltration. On the contrary,

significant deswelling in PMMA films is a clear evidence of the limited reactivity of TMA molecules with the PMMA polymer. Accordingly, *ex-situ* XPS measurements were performed in order to better clarify this point and identify the specific reactive sites involved in the reaction of TMA with PLA and PMMA polymers. The low resolution XPS spectra of pristine and infiltrated PLA and PMMA films are reported in **Figure 4a** and **4b**, respectively. The analysis was restricted to the samples infiltrated using a TMA pulse time of 20 ms and 40 ms. The spectra of the pristine polymer films are characterized by the presence of two main signals at approximately ~285 eV and ~530 eV that correspond to C *1s* and O *1s* core levels, consistently with the chemical structures of the two polymers. The spectra of the infiltrated samples are characterized by two additional peaks at approximately 120 eV and 75 eV, corresponding to Al *2s* and Al *2p* core levels, respectively. These signals confirm effective incorporation of Al_2O_3 into the polymers upon infiltration.[52]

Figure 5a and **5b** report the high resolution XPS spectra (open symbols) of the C *1s* and O *1s* signals obtained from pristine and infiltrated PLA films, respectively. The C *1s* spectrum of pristine PLA film is distinctly characterized by the presence of three main components that well correlate with the chemical structure of the PLA monomer, as highlighted by the coloured semi-transparent circles in the inset of **figure 5a**. These components are labelled as C=OOC, C-OCCH and C-CHHH to account for the nearest neighbours of the specific carbon atom associated to each component. The spectrum of the pristine sample was deconvoluted by fitting experimental data with Voight functions (coloured area) in order to determine the binding energy of the different components. The fitting parameters for the different components of the pristine sample are reported in **table S1**. Similarly, the O *1s* high resolution spectrum of the pristine PLA film was deconvoluted by fitting the experimental data with two Voight functions (coloured solid lines) corresponding to the different chemical configurations of the oxygen atoms in the PLA monomers, as highlighted by coloured semi-transparent circles in the inset of **figure 5b**. Accordingly, these two components have been labelled

as O-CC and O=C to account for the nearest neighbours of the specific oxygen atom associated to each component.

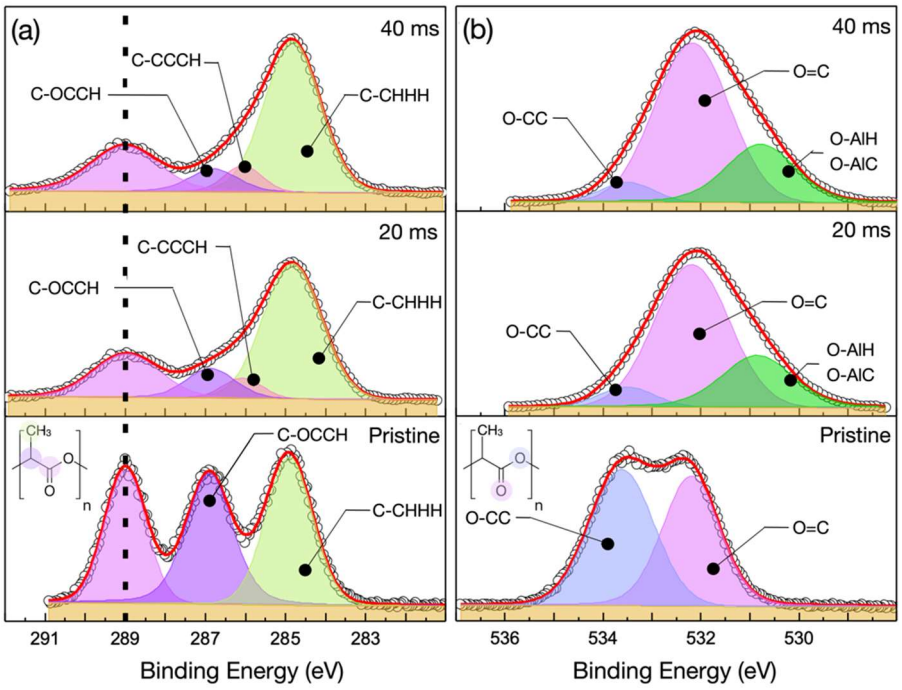

***Figure 5**: High resolution XPS spectra (open symbols) of C 1 (a) and O 1s (b) core levels for pristine and infiltrated 15 nm thick PLA films. Black dashed line indicates the binding energy (289.0 eV) of C 1s core level originated by the carbonyl group that was used as a reference to correct the energy shift of the binding energy induced by charging. In the insets the chemical structure of the pristine PLA molecule with the indication (colored shadows) of the C (a) and O (b) atoms generating the photoelectrons corresponding to the different components of the spectra (colored shadows). Red lines correspond to the best fitting of the experimental data resulting from the convolution of the different components*

The C *1s* and O *1s* spectra of the infiltrated PLA films are significantly modified compared to those of the pristine samples. In particular, the intensities of the C=OOC, C-OCCH components of the C *1s* spectra are much lower than the intensity of the C-CHHH component, suggesting that the ester group is significantly affected by the interaction with the TMA precursors during the infiltration process. Moreover, an additional component was introduced to properly fit the experimental data. Considering the shift of the binding energy with respect to the C-CHHH component, this new component was identified as C-CCCH. The fitting parameters for the different components in the infiltrated samples are reported in **table S1**. Similarly the O *1s* spectra of the infiltrated samples

exhibit a significant reduction of the O-CC component with respect to the O=C component. An additional component O-AlH at low binding energies was introduced in the fitting of the experimental data and associated to the presence of hydroxy groups bonded to Al atoms. An O-AlC component is expected to be present because of the reaction of the O atoms of the ester group with the Al of the TMA precursor. This component is assumed to have binding energy similar to the one of the O-AlH component. The experimental data indicate that the infiltration of Al_2O_3 into the PLA matrix takes place through the reaction of TMA with the ester groups that are present in the polymer chains. In particular Al_2O_3 incorporation appears to be mainly associated to the formation of Al−O bonds between the Al atoms of the TMA precursors and the O atoms of the ether groups, suggesting the occurrence of a polymer chain scission during the TMA reaction as already proposed in the case of TMA reaction with PBS films.[33]

Figure 6a and **6b** show the high resolution XPS spectra of the C *1s* and O *1s* signals obtained from pristine and infiltrated PMMA films, respectively. The C *1s* spectrum of pristine PMMA film is distinctly characterized by the presence of four main components indicated as C=OCC, C-OHHH, C-CCCC and C-CCHH, respectively. The last component overlaps with the C-CHHH component that is expected to be present in the C *1s* spectrum of PMMA, according to the chemical structure of the PMMA monomer that is shown in the inset of **figure 6a**. As in the case of PLA, the O *1s* spectrum of pristine PMMA film is deconvoluted in two components corresponding to O-CC and O=C signals. The fitting parameters for the different components of the C *1s* and O *1s* spectra of the pristine PMMA sample are reported in **table S1**.

The evolution of the C *1s* and O *1s* spectra of the PMMA films upon infiltration is quite similar to the one of PLA. More precisely, the intensities of the C=OOC, C-OHHH components of the C *1s* spectra are much lower than the intensity of the C-CHHH component, suggesting that the ester group is significantly modified because of the interaction with the TMA and H_2O precursors during the infiltration process. Interestingly the C-CCCC component remains fairly constant indicating that the

carbon atom in the polymer backbone is not involved in the reaction with the TAM molecules. The fitting parameters for the different components in the infiltrated samples are reported in **table S1**. Similarly the O *1s* spectra of the infiltrated samples exhibit a reduction of the O-CC component with respect to the O=C component. The reduction of the O-CC component is significantly lower than in the case of PLA, suggesting that only a fraction of the ether groups is consumed during the SIS process. An additional component O-AlH at low binding energies was introduced to account for Al_2O_3 incorporation through the formation of Al−O bonds between the Al atoms of the TMA precursors and the O atoms of the ether groups. The low intensity of this component with respect to the one associated to the O=C group further corroborate the idea of a limited Al_2O_3 incorporation into the PMMA matrix, in perfect agreement with the results obtained by *operando* SE measurements.

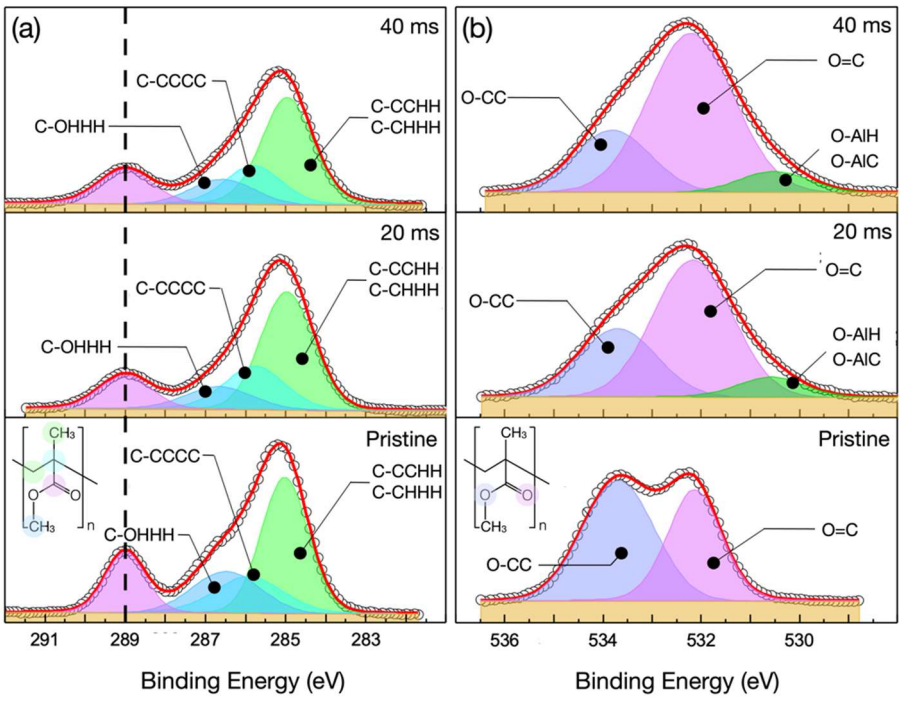

Figure 6: *High resolution XPS spectra (open symbols) of C 1 (a) and O 1s (b) core levels for pristine and infiltrated 15 nm thick PMMA films. Black dashed line indicates the binding energy (289.0 eV) of C 1s core level originated by the carbonyl group that was used as a reference to correct the energy shift of the binding energy induced by charging. In the insets the chemical structure of the pristine PMMA molecule with the indication (colored shadows) of the C (a) and O (b) atoms generating the photoelectrons corresponding to the different components of the spectra (colored shadows). Red lines correspond to the best fitting of the experimental data resulting from the convolution of the different components.*

Density Functional Theory Results

Interaction Between TMA and PMMA and PLA Polymers. The infiltration chemistry of TMA into PMMA has previously been studied by density functional theory (DFT) using a gas phase monomer as the model polymer.[26,53] Our investigated reaction path followed that described for TMA in PMMA from the work of Dandley et al.[53] In this proposed reaction path, TMA initially forms an adduct with a C=O group in PMMA, yielding a redshift of 65 cm^{-1} in the IR-peak for the C=O stretch and a blueshift of 15-25 cm^{-1} for the C-O IR modes.[53] From this TMA interaction site, TMA can then decompose by methyl transfer or insertion into the ester bond, yielding further shifts in the C=O and C-O IR-peaks.

In our model system, TMA forms an adduct through an interaction with the C=O group present in PMMA and PLA and these adducts show similar structures, as seen in **Figure 7(a)** and **7(b)**. The formation of the adduct is weakly exothermic for both polymers, being -0.44 eV for PLA and -0.59 eV for PMMA. The relatively small interaction energy and the lack of any covalent bond breaking or forming indicates that the interaction of TMA at both polymers can be reversible, with bound TMA potentially being easily released from the polymer through the purge step in an SIS cycle. Further reactions of TMA are needed for it to bind strongly to the polymer so that it is not released during purging. Upon forming the adduct the C=O distance lengthens from 1.20 Å to 1.22 Å in both PLA and PMMA. The TMA molecule adopts a slightly tetrahedral arrangement, with no covalent modifications occurring in either polymer. The most noticeable difference between the adduct structures for both polymers is the distance of the TMA to the backbone of the polymer. TMA is much closer to the polymer backbone in PLA than in PMMA, as the C=O group lies in the PLA backbone compared to its position in a sidechain in PMMA.

Figure 8 shows the computed IR spectra for PMMA and PLA without and with TMA adduct. The dominant change in the IR spectra after forming the adduct is a redshift of the C=O stretch mode that is 77.45 cm^{-1} for PLA and 66.55 cm^{-1} for PMMA. The value of the redshift value for PMMA agrees well with the previous calculated value of 65 cm^{-1}.[53] and the similar, but larger, magnitude for PLA is consistent with similarities in the TMA-polymer interaction mode and differences in adduct geometry and binding strength.

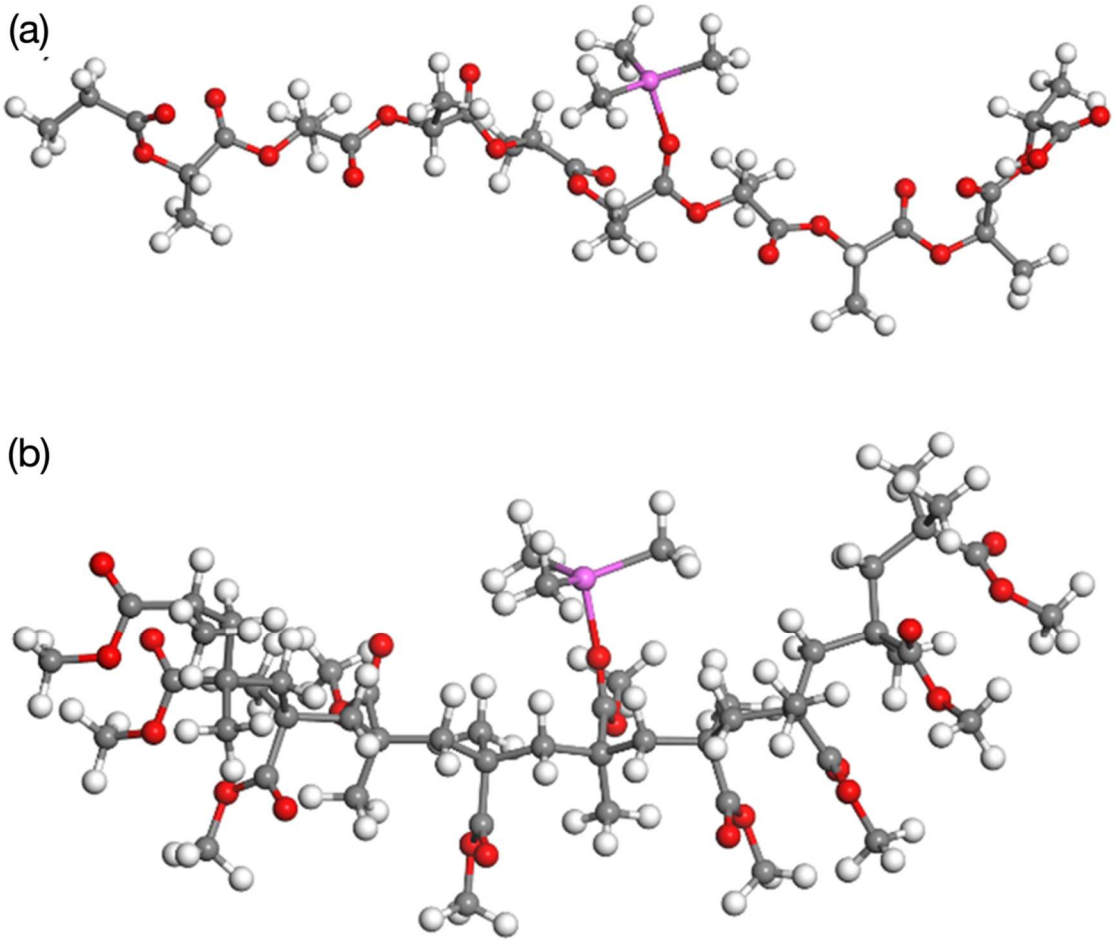

Figure 7: *Optimized geometry of TMA forming an adduct with (A) PLA and (B) PMMA. Carbon atoms are grey, hydrogen are white, oxygen are red, and aluminium are magenta.*

The two different decomposition pathways for the TMA adduct were then investigated using this non-periodic model. A methyl transfer product is stable for both PLA and PMMA polymers as seen in **Figure 9(a)** and **9(b)**. In PLA the produced dimethyl aluminium (DMA) coordinates to an oxygen atom in a neighbouring C=O in the polymer backbone, while the methyl group is migrated to

the carbon centre of the initial C=O group. The same coordination cannot occur in PMMA due to neighbouring C=O moieties being further away, with the dimethyl only binding to the initial C=O oxygen and the methyl group to the carbon. For methyl transfer in PLA the IR peak for the C=O stretch mode of the coordinating carbonyl is redshifted by 125 cm^{-1} indictive of DMA forming a stronger coordination compared to TMA. The redshifted C=O IR peak from the adduct disappears as the bond order is reduced and a new IR peak at 1353.47 cm^{-1} appears corresponding to the new C-O stretch, as shown in **Figure 8**.

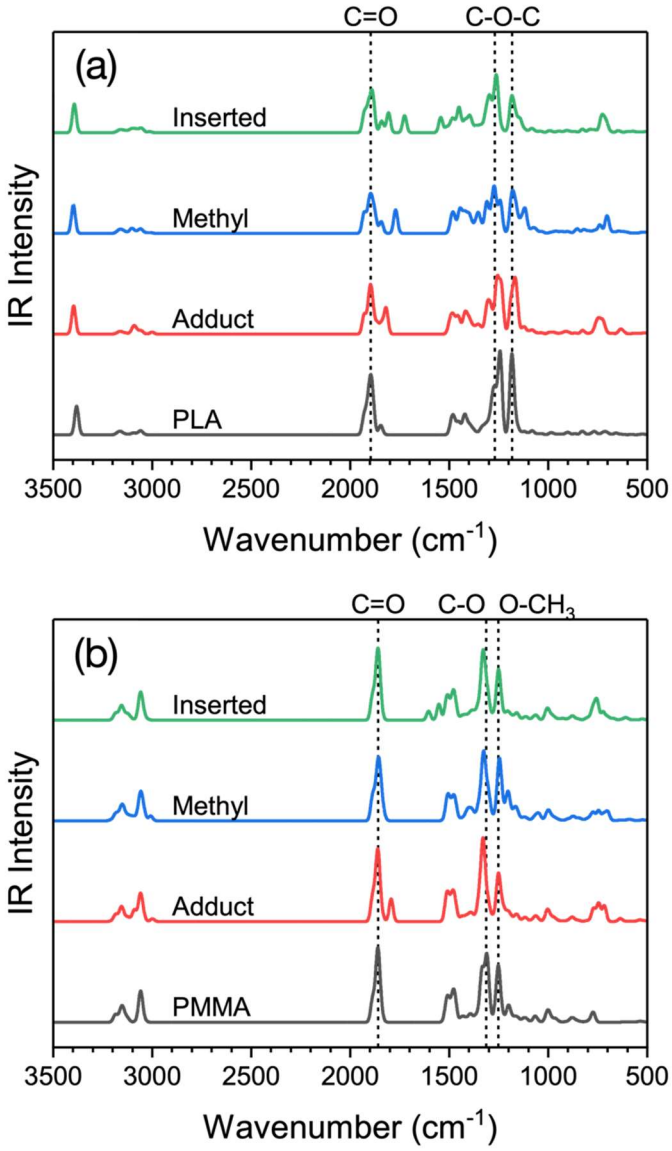

Figure 8: *Calculated IR spectra of pristine polymer and with an TMA adduct, methyl shifted TMA and inserted TMA for PLA (a) and PMMA (b).*

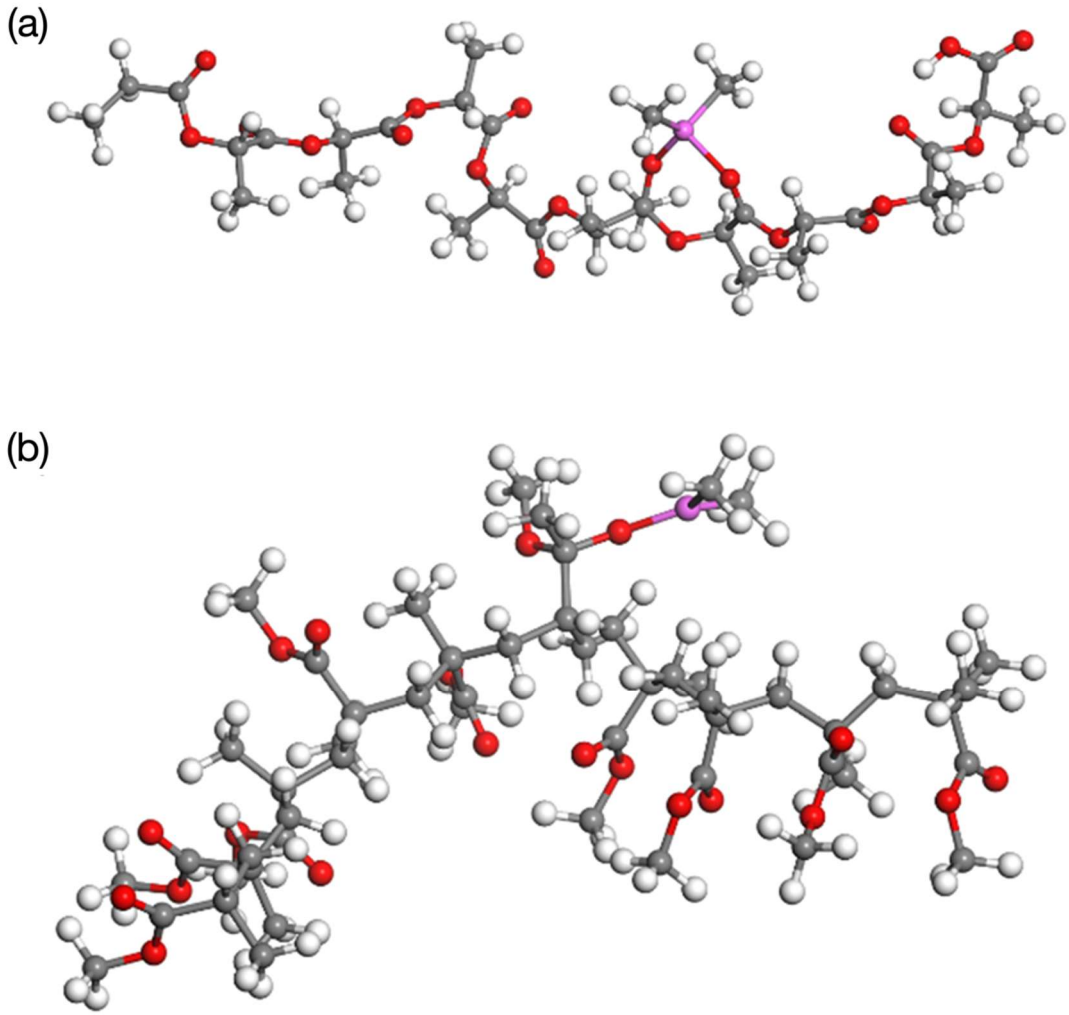

Figure 9: *Optimized geometry of the methyl transfer product for PLA (a) and PMMA (b). Carbon atoms are grey, hydrogen are white, oxygen are red, and aluminium are magenta.*

The methyl transfer reaction is exothermic for PLA with a reaction energy of -1.44 eV relative to the adduct formation, while the reaction was endothermic for PMMA with a reaction energy of 0.16 eV relative to the adduct. This agrees with previous conclusions that the methyl transfer is not a viable reaction when TMA interacts at PMMA and the TMA:C=O adduct is a more preferred interaction mode with PMMA.

The second investigated reaction path was insertion of TMA after the ester oxygen. This product was found for both polymers, however the difference in location of the C=O group between PLA and PMMA strongly influences the final geometry of the product, as shown in **Figure 10**. When

TMA is inserted into PLA, the backbone of the polymer is severed as the DMA chelates to the two oxygen atoms on the carboxyl terminal, while a methyl group is transferred to the carbon-head of the fragment chain. The chain is however able to reattach due to the DMA group crosslinking the two fragments. The insertion reaction is more exothermic than methyl transfer with a reaction energy -2.56 eV relative to the adduct, while breaking the crosslink between the two fragments is endothermic with an energy cost of 0.62 eV. The most notable change in the IR spectrum for TMA insertion into PLA is a redshift of 89.66 cm^{-1} for the C=O stretch mode of the crosslinked oxygen and the addition of two new peaks at 1725.42 cm^{-1} and 1542.98 cm^{-1} corresponding to asymmetrical and symmetrical stretch modes of the chelating carboxyl terminal.

For PMMA the polymer backbone remains intact after TMA insertion, due the location of the C=O moiety of the sidechain. However, an ethane molecule is released from the polymer upon insertion. This reaction is also exothermic, albeit less so than for PLA, with a reaction energy of -1.82 eV relative to the adduct. The peak corresponding to the redshifted C=O stretch disappears from the IR spectra upon insertion and two peaks, corresponding to the asymmetrical and symmetrical stretch mode of the chelating carboxyl group, appears at 1604.34 cm^{-1} and 1152.11 cm^{-1} respectively.

Figure 11 shows a scheme summarizing the reaction pathways of TMA with PMMA and PLA. In both cases the formation of an adduct between the TMA molecule and the C=O moiety is found to be a weakly exothermic reaction that is expected to be reversible at room temperature. Two possible reactions paths are investigated with a methyl transfer between TMA and the polymer chain or the insertion of the TMA molecule into the polymer chain by reaction with the ester oxygen. The methyl transfer reaction is determined to be endothermic for PMMA and exothermic for PLA, indicating this is not a viable path for TMA reaction with PMMA. The more favourable reaction energy for TMA insertion into PLA compared to PMMA is consistent with the experimental XPS, with a stronger reduction in the C-O intensity for PLA compared with PMMA.

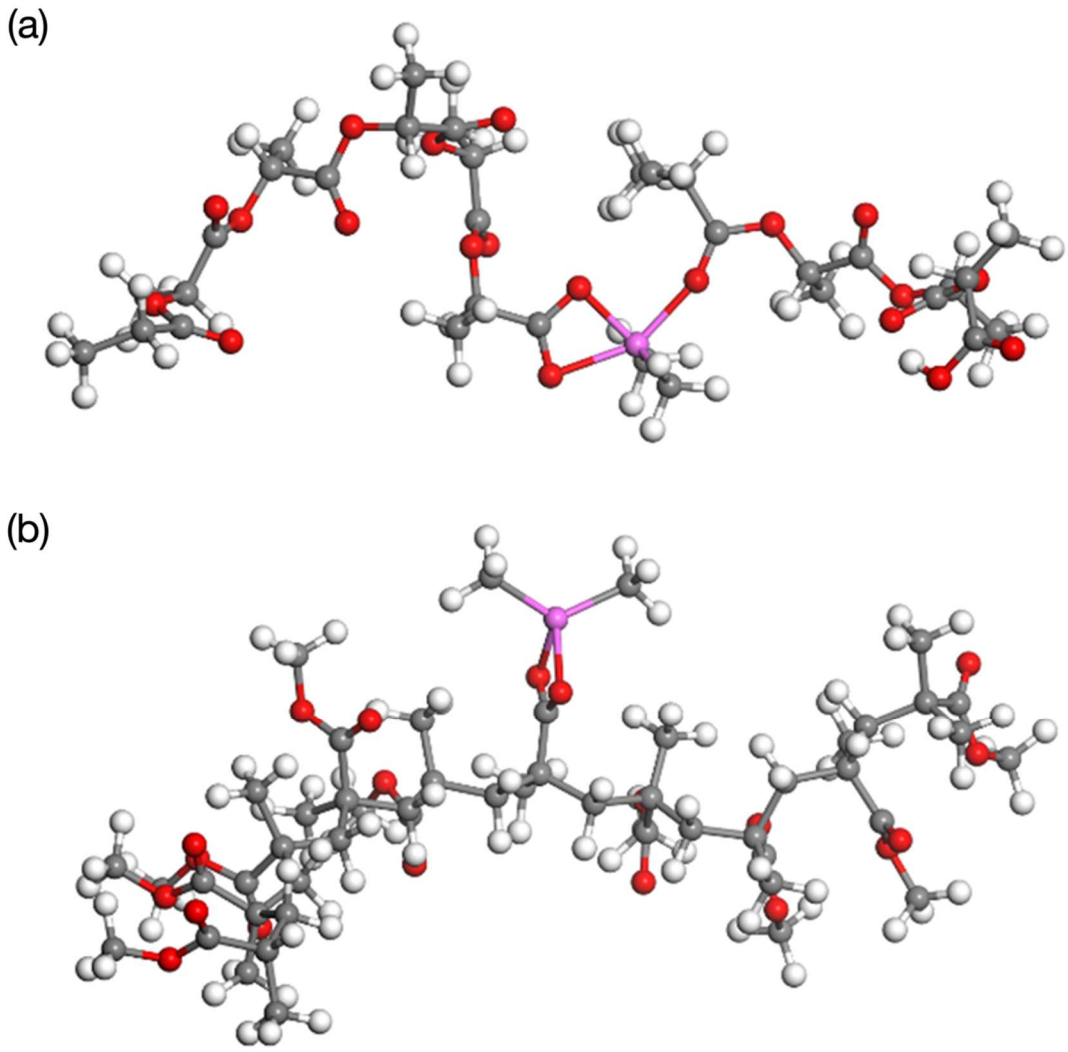

Figure 10: *Optimized geometry of the TMA insertion product for PLA (a) and PMMA (b). Carbon atoms are grey, hydrogen are white, oxygen are red, and aluminium are magenta.*

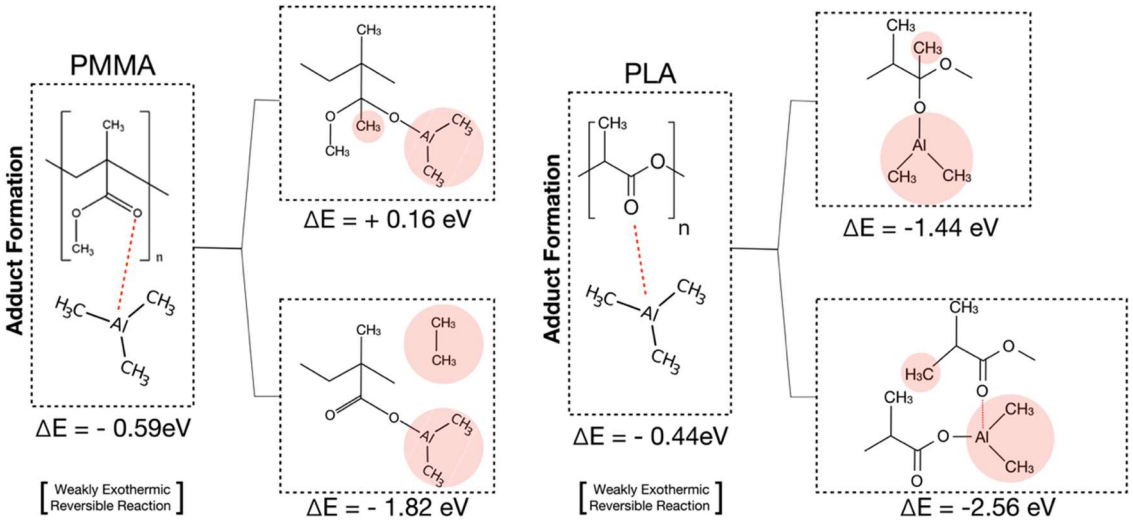

Figure 11*: scheme showing the reaction path of PMMA and PLA with a TMA molecule. Irrespective of the final reaction products, the reaction path goes through the formation of an adduct between the carboxylic group and the TMA molecule via a weakly exothermic reaction.*

Swelling of TMA-Infiltrated Polymers. The atomic structure of the polymers together with the volume and the shape of the computational cell were optimized without any TMA introduced and the density of the polymers is calculated. For PLA the calculated density is 1.180 g cm^{-3}, close to the experimental density 1.25 g cm^{-3}. The calculated PMMA density was 1.232 g cm^{-3} with the experimental density of 1.17 – 1.20 g cm^{-3}. The close agreement with experimental density indicates that the model can be used to estimate the swelling upon infiltration of TMA.

TMA infiltration was modelled by adding an increasing number of TMA molecules into the polymer supercell, up to a maximum of one TMA per monomer (16 TMA molecules) and optimizing the structure and volume. The TMA molecules were initially placed in close proximity to the C=O groups in the polymers to allow formation of the adduct structure found in the non-periodic model. The infiltration energy, optimized volume of the cell and computed swelling are given in **Table S2** and the optimized geometry for the polymers with 2, 8 and 16 TMA infiltrated are shown in **Figure 12.**

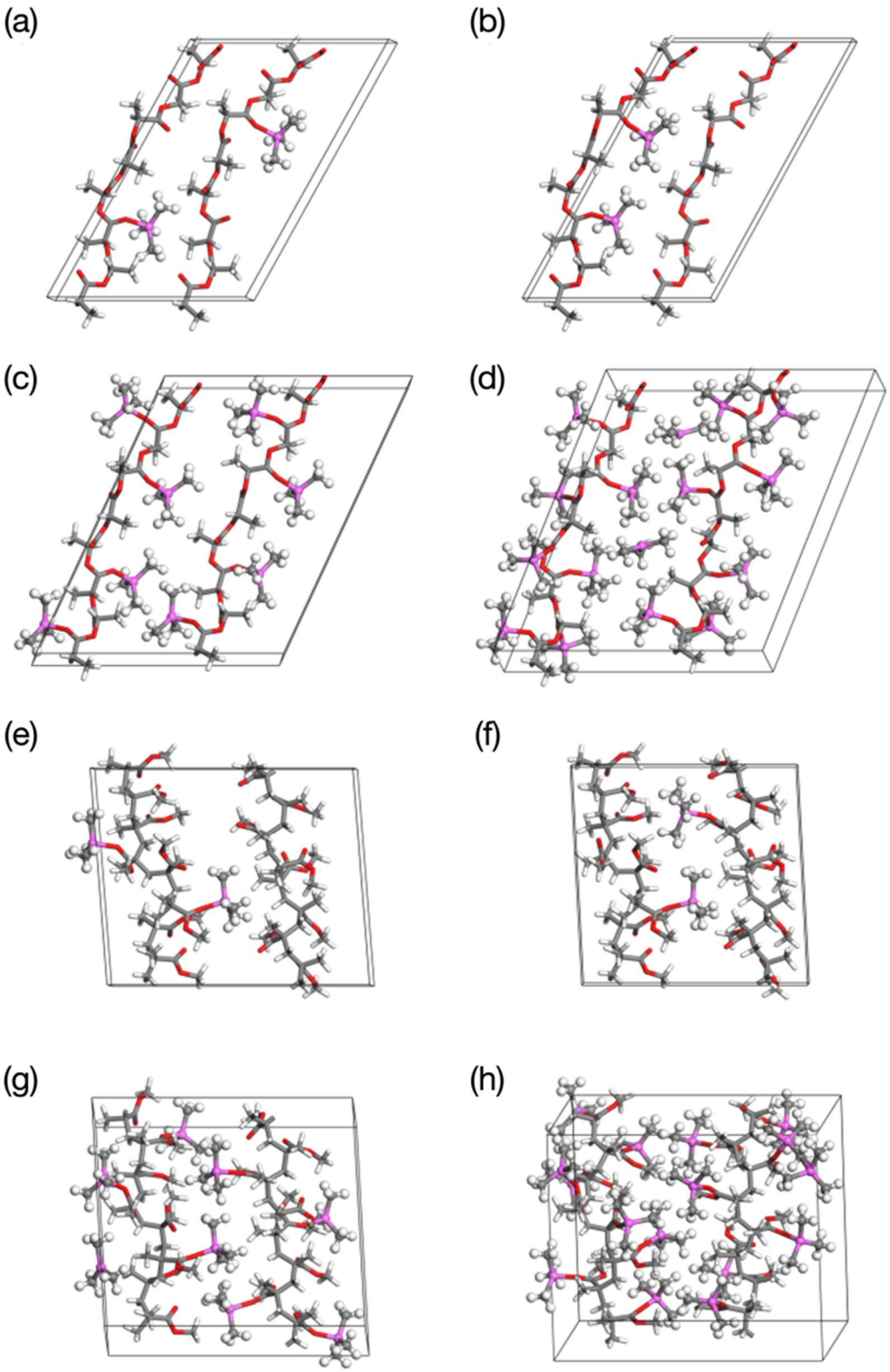

Figure 12: *Optimized geometry of PLA (a-d) and PMMA(e-h) with 2, 8 and 16 infiltrated TMA molecules. The "near" configurations of two TMA molecules are shown in (a) and (e), and the "far" are shown in (b) and (f). Carbon atoms are grey, hydrogen are white, oxygen are red, and aluminum are magenta.*

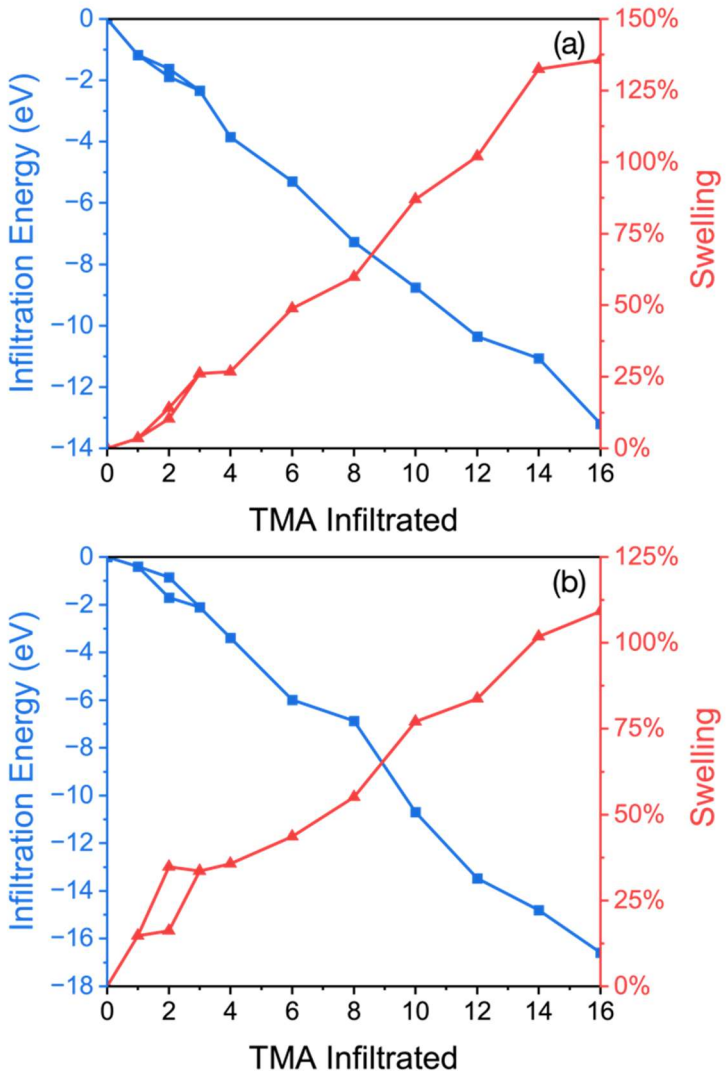

Figure 13: *Infiltration energy and swelling for an increasing amount of infiltrated TMA (measured by the number of TMA molecules added) into PLA (a) and PMMA (b).*

For two TMA molecules infiltration was investigated at two different positions in the supercell. In one model the two TMA molecules are placed close to each other at the same polymer chain and the other model has the two TMA molecules placed far apart, at different polymer chains. The infiltration energy for the TMA molecules follows a generally linear relation for both polymers, as seen in **Figure 13**, indicating that the binding energy for the TMA to the polymer is independent of saturation level. The average binding energies were calculated to be -0.84 eV for PLA and -1.03 eV for PMMA. The slightly stronger adduct formation energy for PMMA compared to PLA agrees well with the non-periodic model.

Although both polymers showed swelling upon infiltration of TMA, they show different behavior. Swelling in PLA followed a generally linear trend starting from 1 TMA, with an average swelling of 8.6 % per TMA and reaching a maximum swelling of 136 % at saturation. For PMMA the swelling for the initial two TMA infiltration was much higher, on average 16.8 %. Upon addition of more TMA the swelling was lower, leading to an average swelling of 7.3 % / TMA to and reaching a maximum swelling of 109 % at saturation.

The linear swelling and initially lower magnitude of swelling observed in PLA can stem from the polymer chain being flexible and it can therefore distort its structure to accommodate the introduced TMA molecules. The PMMA chains are more rigid and, instead of distorting around the TMA, they initially separate to accommodate the adduct. The two different infiltration positions of two TMA in PMMA is consistent with a more rigid polymer. When an additional TMA molecule is infiltrated close to a TMA adduct the already created void allows for the second TMA molecule to fit, and only a small swelling is observed. In contrast, if the second TMA molecule is infiltrated far from the original TMA-polymer adduct, the structure must swell to the same degree as the initial infiltration to fit the additional TMA molecule. This explains the large initial swelling and the subsequently lower swelling afterwards - the first TMA molecules separates the PMMA chains creating voids that the following TMA molecules can fit into.

Phonon (vibrational) density of states (VDOS) of pristine and TMA infiltrated PLA and PMMA were calculated using a smaller six monomer, single chain periodic mode. The smaller model gave similar results for swelling and infiltration energy compared to the larger model, for details see supporting information. As with the IR spectrum, the VDOS shows a redshift of the C=O stretch mode corresponding to the adduct location, as highlighted in **Figure 14**. The location of the shifted and unshifted peaks are mostly independent of the amount of infiltrated TMA, except for small shifts due to minor structural changes upon adduct formation, and the main difference in the PDOS upon TMA infiltration is the relative size of the two peaks. The average redshift is 45.40 cm^{-1} for PLA and

70.26 cm^{-1} for PMMA, consistent with other results for the shift in this vibrational mode upon adduct formation.

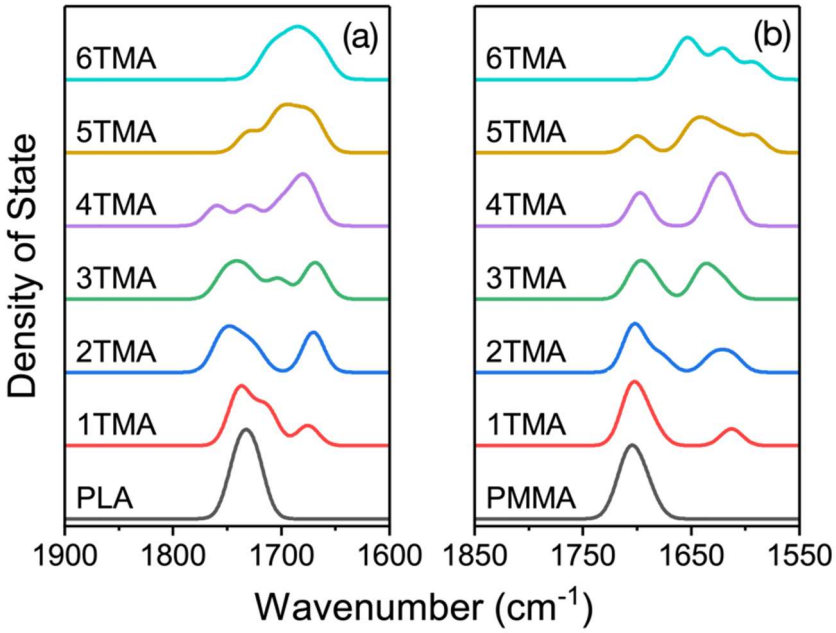

Figure 14: *Section of phonon density of states (PDOS) for PLA (a) and PMMA (b) with increasing number of infiltrated TMA molecules, highlighting the C=O stretch mode. Full PDOS is given as Figure S1 in the supporting information.*

The six-monomer model was also used to investigate the TMA insertion reaction in a periodic model. Insertion of one, two and three TMA molecules, corresponding to insertion into half of the monomers, were modelled. Optimized geometries for the insertion product of three TMA molecules are shown in **Figure 15**. Similar to the non-periodic model, the PLA chain was severed upon TMA insertion and reattached via the DMA. The placement of the DMA product along the polymer backbone would allow further TMA molecules to diffuse through the polymer to find other binding sites. For PMMA the location of DMA on the sidechain allowed it larger mobility and was able to form adducts with adjacent C=O groups, both on the same chain and on neighboring chains. This would form a crosslinked network of polymer chains and both block binding sites for additional TMA and hinder diffusion of TMA into the polymer, so that the TMA-C=O adduct would dominate. This

yields a smaller swelling in PMMA and the observed reduction in swelling seen experimentally upon purging

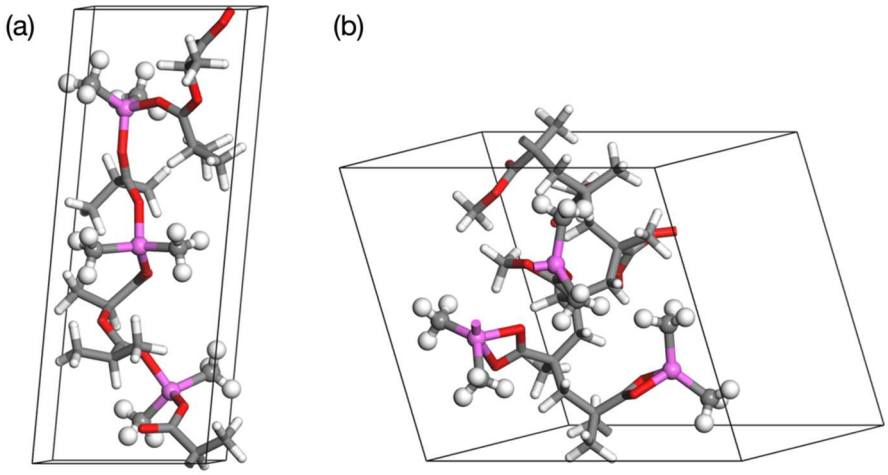

Figure 15: *Optimized geometry for the insertion product of three TMA molecules for PLA (A) and PMMA (D). Two of the DMA fragments crosslink with other C=O groups over the periodic boundary for PMMA. Carbon atoms are grey, hydrogen are white, oxygen are red, and aluminum are magenta.*

Conclusions

In this work, Al_2O_3 was infiltrated in PMMA and poly PLA thin films with an ALD reactor, operating at 70°C in quasi-static mode, using TMA and H_2O. These polymers are characterized by the presence of ester groups along the polymer chain that are expected to act as reactive sites for TMA. *Operando* spectroscopic ellipsometry revealed that significant swelling and deswelling of PMMA occurs during TMA exposure and purging, respectively, due to sorption and subsequent desorption of TMA molecules that are not stably incorporated into the PMMA matrix. PLA exhibited a much larger swelling than PMMA during TMA exposure, but no significant deswelling was observed during purging, suggesting that a large amount of infiltrated TMA molecules can be effectively trapped into the polymer matrix by a stable chemical bond. Accordingly, *ex-situ* XPS analysis demonstrated that much more Al_2O_3 is grown in PLA than in PMMA. The *ex-situ* XPS analysis also shows that, in both polymers TMA incorporation mainly occurs through the formation

of an Al-O covalent bond at the C-O-C group, similar to other biopolymers. Two density functional theory (DFT) approaches were used to investigate the infiltration of TMA into PMMA and PLA. Binding configurations, energies and vibrational spectra were modelled using a gas phase model of a ten-unit oligomer. For both polymers, TMA forms an adduct with the oxygen in the C=O with an exothermic reaction energy, consistent with experiment. Furthermore, TMA was able to exothermically insert into the C-O-C bond of PLA, forming a covalent Al-O bond, aligning with the *ex-situ* XPS results. Infiltration modelling employed a periodic model from which we show that PMMA and PLA swell upon TMA infiltration, saturating with increasing TMA, consistent with experimental findings. This combined experimental and theoretical study provides deeper insights into SIS of Al_2O_3 in PMMA and PLA. This methodology can be extended to other precursors and polymer pairs, allowing the unravelling of the complexities of SIS at the molecular level.

Acknowledgments

The authors would like to thank Stefano Tagliabue (Corapack®) for providing the PLA films. This research was partially supported by the project "sPATIALS3", financed by the European Regional Development Fund under the ROP of the Lombardy Region ERDF 2014−2020 - Axis I "Strengthen technological research, development and innovation"- Action 1.b.1.3 "Support for co- operative R&D activities to develop new sustainable technologies, products and services" - Call Hub. The research reported in this publication was also funded by the Irish Research Council under grant number GOIPD/2023/1099 and from the Foundation for Bengt Lundqvist's memory. Computational resources and support were provided from the Irish Centre for High-End Computing (ICHEC).

Supporting information: fitting parameters of the high resolution XPS spectra, infiltration energy, volume, swelling and lattice constants for infiltrated PLA and PMMA, phonon density of states for infiltrated PLA and PMMA.

References

(1) Lee, S.-M.; Pippel, E.; Gösele, U.; Dresbach, C.; Qin, Y.; Chandran, C. V.; Bräuniger, T.; Hause, G.; Knez, M. Greatly Increased Toughness of Infiltrated Spider Silk. *Science* **2009**, *324* (5926), 488–492. https://doi.org/10.1126/science.1168162.

(2) Peng, Q.; Tseng, Y.; Darling, S. B.; Elam, J. W. Nanoscopic Patterned Materials with Tunable Dimensions via Atomic Layer Deposition on Block Copolymers. *Adv. Mater.* **2010**, *22* (45), 5129–5133. https://doi.org/10.1002/adma.201002465.

(3) Dandley, E. C.; Lemaire, P. C.; Zhu, Z.; Yoon, A.; Sheet, L.; Parsons, G. N. Wafer-Scale Selective-Area Deposition of Nanoscale Metal Oxide Features Using Vapor Saturation into Patterned Poly(Methyl Methacrylate) Templates. *Adv. Mater. Interfaces* **2016**, *3* (2), 1500431. https://doi.org/10.1002/admi.201500431.

(4) Leng, C. Z.; Losego, M. D. Vapor Phase Infiltration (VPI) for Transforming Polymers into Organic–Inorganic Hybrid Materials: A Critical Review of Current Progress and Future Challenges. *Mater. Horiz.* **2017**, *4* (5), 747–771. https://doi.org/10.1039/C7MH00196G.

(5) Yurkevich, O.; Modin, E.; Šarić Janković, I.; Peter, R.; Petravić, M.; Knez, M. Introducing a Robust Flexible Conductive Hybrid: Indium Oxide-ParyleneC Obtained by Vapor Phase Infiltration. *Chem. Mater.* **2023**, *35* (18), 7529–7541. https://doi.org/10.1021/acs.chemmater.3c01115.

(6) Gong, B.; Parsons, G. N. Quantitative in Situ Infrared Analysis of Reactions between Trimethylaluminum and Polymers during Al2O3 Atomic Layer Deposition. *J. Mater. Chem.* **2012**, *22* (31), 15672. https://doi.org/10.1039/c2jm32343e.

(7) Subramanian, A.; Tiwale, N.; Lee, W.; Kisslinger, K.; Lu, M.; Stein, A.; Kim, J.; Nam, C. Vapor-Phase Infiltrated Organic–Inorganic Positive-Tone Hybrid Photoresist for Extreme UV

Lithography. *Adv. Mater. Interfaces* **2023**, *10* (28), 2300420. https://doi.org/10.1002/admi.202300420.

(8) Tiwale, N.; Subramanian, A.; Kisslinger, K.; Lu, M.; Kim, J.; Stein, A.; Nam, C.-Y. Advancing next Generation Nanolithography with Infiltration Synthesis of Hybrid Nanocomposite Resists. *J. Mater. Chem. C* **2019**, *7* (29), 8803–8812. https://doi.org/10.1039/C9TC02974E.

(9) Baryshnikova, M.; De Simone, D.; Knaepen, W.; Kachel, K.; Chan, B.; Paolillo, S.; Willem Maes, J.; De Roest, D.; Rincon Delgadillo, P.; Vandenberghe, G. Sequential Infiltration Synthesis for Line Edge Roughness Mitigation of EUV Resist. *J. Photopolym. Sci. Technol.* **2017**, *30* (6), 667–670. https://doi.org/10.2494/photopolymer.30.667.

(10) Barrows, F.; Arava, H.; Zhou, C.; Nealey, P.; Segal-Peretz, T.; Liu, Y.; Bakaul, S.; Phatak, C.; Petford-Long, A. Mesoscale Confinement Effects and Emergent Quantum Interference in Titania Antidot Thin Films. *ACS Nano* **2021**, *15* (8), 12935–12944. https://doi.org/10.1021/acsnano.1c01340.

(11) Seguini, G.; Motta, A.; Bigatti, M.; Caligiore, F. E.; Rademaker, G.; Gharbi, A.; Tiron, R.; Tallarida, G.; Perego, M.; Cianci, E. Al_2O_3 Dot and Antidot Array Synthesis in Hexagonally Packed Poly(Styrene- *Block* -Methyl Methacrylate) Nanometer-Thick Films for Nanostructure Fabrication. *ACS Appl. Nano Mater.* **2022**, *5* (7), 9818–9828. https://doi.org/10.1021/acsanm.2c02013.

(12) Michelson, A.; Subramanian, A.; Kisslinger, K.; Tiwale, N.; Xiang, S.; Shen, E.; Kahn, J. S.; Nykypanchuk, D.; Yan, H.; Nam, C.-Y.; Gang, O. Three-Dimensional Nanoscale Metal, Metal Oxide, and Semiconductor Frameworks through DNA-Programmable Assembly and Templating. *Sci. Adv.* **2024**, *10* (2), eadl0604. https://doi.org/10.1126/sciadv.adl0604.

(13) Mu, X.; Wang, W.; Sun, C.; Zhao, D.; Ma, C.; Zhu, J.; Knez, M. Greatly Increased Electrical Conductivity of PBTTT-C14 Thin Film via Controllable Single Precursor Vapor Phase Infiltration. *Nanotechnology* **2023**, *34* (1), 015709. https://doi.org/10.1088/1361-6528/ac96fa.

(14) Mariello, M.; Von Allmen, M.; Wu, K.; Van Gompel, M.; Lacour, S. P.; Leterrier, Y. Hermetic, Hybrid Multilayer, Sub-5µm-Thick Encapsulations Prepared with Vapor-Phase Infiltration of Metal Oxides in Conformal Polymers for Flexible Bioelectronics. *Adv. Funct. Mater.* **2024**, 2403973. https://doi.org/10.1002/adfm.202403973.

(15) Chamorro, N.; Azpitarte, I.; Autore, M.; Ablat, H.; Saric Jankovic, I.; Amenabar, I.; Tollan, C.; Vavassori, P.; Hillenbrand, R.; Elliott, S.; Knez, M. Matrix Doping of ZnO and In_2O_3 in Para-Aramid via Vapor Phase Infiltration for Enhanced Electronic Properties. *ACS Appl. Polym. Mater.* **2024**, *6* (17), 10592–10602. https://doi.org/10.1021/acsapm.4c00657.

(16) Zhou, C.; Segal-Peretz, T.; Oruc, M. E.; Suh, H. S.; Wu, G.; Nealey, P. F. Fabrication of Nanoporous Alumina Ultrafiltration Membrane with Tunable Pore Size Using Block Copolymer Templates. *Adv. Funct. Mater.* **2017**, *27* (34), 1701756. https://doi.org/10.1002/adfm.201701756.

(17) Barry, E.; Mane, A. U.; Libera, J. A.; Elam, J. W.; Darling, S. B. Advanced Oil Sorbents Using Sequential Infiltration Synthesis. *J. Mater. Chem. A* **2017**, *5* (6), 2929–2935. https://doi.org/10.1039/C6TA09014A.

(18) Simon, A.; Zhang, Z.; Abetz, C.; Abetz, V.; Segal-Peretz, T. Atomic Layer Deposition Enables Multi-Modal Three-Dimensional Electron Microscopy of Isoporous Membranes. *Nanoscale* **2023**, *15* (7), 3219–3229. https://doi.org/10.1039/D2NR05477A.

(19) Shevate, R.; Rozyyev, V.; Pathak, R.; Mane, A. U.; Sankhala, K.; Gao, F.; Segal-Peretz, T.; Darling, S. B.; Elam, J. W. Tailoring the Interfacial Interactions of Porous Polymer Membranes to Accelerate Atomic Layer Deposition: The Latent Path to Antifouling Membranes. *Chem. Mater.* **2024**, *36* (8), 3616–3627. https://doi.org/10.1021/acs.chemmater.3c03090.

(20) Waldman, R. Z.; Mandia, D. J.; Yanguas-Gil, A.; Martinson, A. B. F.; Elam, J. W.; Darling, S. B. The Chemical Physics of Sequential Infiltration Synthesis—A Thermodynamic and Kinetic Perspective. *J. Chem. Phys.* **2019**, *151* (19), 190901. https://doi.org/10.1063/1.5128108.

(21) Waldman, R. Z.; Jeon, N.; Mandia, D. J.; Heinonen, O.; Darling, S. B.; Martinson, A. B. F. Sequential Infiltration Synthesis of Electronic Materials: Group 13 Oxides via Metal Alkyl Precursors. *Chem. Mater.* **2019**, *31* (14), 5274–5285. https://doi.org/10.1021/acs.chemmater.9b01714.

(22) Cara, E.; Murataj, I.; Milano, G.; De Leo, N.; Boarino, L.; Ferrarese Lupi, F. Recent Advances in Sequential Infiltration Synthesis (SIS) of Block Copolymers (BCPs). *Nanomaterials* **2021**, *11* (4), 994. https://doi.org/10.3390/nano11040994.

(23) Cai, R.; Weisbord, I.; Caspi, S.; Naamat, L.; Kornblum, L.; Dana, A. G.; Segal-Peretz, T. Rational Design and Fabrication of Block Copolymer Templated Hafnium Oxide Nanostructures. *Chem. Mater.* **2024**, *36* (3), 1591–1601. https://doi.org/10.1021/acs.chemmater.3c02836.

(24) Leng, C. Z.; Losego, M. D. A Physiochemical Processing Kinetics Model for the Vapor Phase Infiltration of Polymers: Measuring the Energetics of Precursor-Polymer Sorption, Diffusion, and Reaction. *Phys. Chem. Chem. Phys.* **2018**, *20* (33), 21506–21514. https://doi.org/10.1039/C8CP04135K.

(25) Ren, Y.; McGuinness, E. K.; Huang, C.; Joseph, V. R.; Lively, R. P.; Losego, M. D. Reaction–Diffusion Transport Model to Predict Precursor Uptake and Spatial Distribution in Vapor-Phase Infiltration Processes. *Chem. Mater.* **2021**, *33* (13), 5210–5222. https://doi.org/10.1021/acs.chemmater.1c01283.

(26) Biswas, M.; Libera, J. A.; Darling, S. B.; Elam, J. W. New Insight into the Mechanism of Sequential Infiltration Synthesis from Infrared Spectroscopy. *Chem. Mater.* **2014**, *26* (21), 6135–6141. https://doi.org/10.1021/cm502427q.

(27) Cianci, E.; Nazzari, D.; Seguini, G.; Perego, M. Trimethylaluminum Diffusion in PMMA Thin Films during Sequential Infiltration Synthesis: In Situ Dynamic Spectroscopic Ellipsometric Investigation. *Adv. Mater. Interfaces* **2018**, *5* (20), 1801016.

(28) Motta, A.; Seguini, G.; Wiemer, C.; Perego, M. Sequential Infiltration Synthesis of Al_2O_3 in PMMA Thin Films: Temperature Investigation by Operando Spectroscopic Ellipsometry. *ACS Appl. Mater. Interfaces* **2024**, *16* (27), 35825–35833. https://doi.org/10.1021/acsami.4c06887.

(29) Perego, M.; Seguini, G.; Wiemer, C.; Caligiore, F. E.; Cianci, E. Al2O3 Growth in PMMA Thin Films by Sequential Infiltration Synthesis: In Situ Thickness Evolution and Mass Uptake Investigation. *Mater. Adv.* **2024**, *5* (9), 3992–3997. https://doi.org/10.1039/D3MA01159C.

(30) McCallum, F.; Hossain, Md. D.; Blakey, I.; Peng, H.; Whittaker, A. K. Revealing the Chemical Interactions between PMMA and TMA for Insights into Sequential Infiltration Synthesis. *Macromolecules* **2024**, acs.macromol.4c01345. https://doi.org/10.1021/acs.macromol.4c01345.

(31) Petit, R. R.; Li, J.; Van De Voorde, B.; Van Vlierberghe, S.; Smet, P. F.; Detavernier, C. Atomic Layer Deposition on Polymer Thin Films: On the Role of Precursor Infiltration and Reactivity. *ACS Appl. Mater. Interfaces* **2021**, *13* (38), 46151–46163. https://doi.org/10.1021/acsami.1c12933.

(32) Biswas, M.; Libera, J. A.; Darling, S. B.; Elam, J. W. Polycaprolactone: A Promising Addition to the Sequential Infiltration Synthesis Polymer Family Identified through *In Situ* Infrared Spectroscopy. *ACS Appl. Polym. Mater.* **2020**, *2* (12), 5501–5510. https://doi.org/10.1021/acsapm.0c00855.

(33) Motta, A.; Seguini, G.; Perego, M.; Consonni, R.; Boccia, A. C.; Ambrosio, G.; Baratto, C.; Cerruti, P.; Lavorgna, M.; Tagliabue, S.; Wiemer, C. Sequential Infiltration Synthesis of Al_2O_3 in Biodegradable Polybutylene Succinate: Characterization of the Infiltration Mechanism. *ACS Appl. Polym. Mater.* **2022**, *4* (10), 7191–7203. https://doi.org/10.1021/acsapm.2c01073.

(34) Padbury, R. P.; Jur, J. S. Temperature-Dependent Infiltration of Polymers during Sequential Exposures to Trimethylaluminum. *Langmuir* **2014**, *30* (30), 9228–9238. https://doi.org/10.1021/la501679f.

(35) Mai, L.; Maniar, D.; Zysk, F.; Schöbel, J.; Kühne, T. D.; Loos, K.; Devi, A. Influence of Different Ester Side Groups in Polymers on the Vapor Phase Infiltration with Trimethyl Aluminum. *Dalton Trans.* **2022**, *51* (4), 1384–1394. https://doi.org/10.1039/D1DT03753F.

(36) Sasao, N.; Sugimura, S.; Asakawa, K.; Oshikiri, T.; Nakagawa, M. Volume Compensating Materials after Vapor Phase Infiltration: Effect of Different Butyl Isomers of Polymer Side-Chains on High Process Temperature Durability. *Jpn. J. Appl. Phys.* **2024**, *63* (4), 04SP14. https://doi.org/10.35848/1347-4065/ad2977.

(37) Padbury, R. P.; Jur, J. S. Comparison of Precursor Infiltration into Polymer Thin Films via Atomic Layer Deposition and Sequential Vapor Infiltration Using *in-Situ* Quartz Crystal Microgravimetry. *J. Vac. Sci. Technol. Vac. Surf. Films* **2014**, *32* (4), 041602. https://doi.org/10.1116/1.4882654.

(38) Jacobs, T.; Declercq, H.; De Geyter, N.; Cornelissen, R.; Dubruel, P.; Leys, C.; Beaurain, A.; Payen, E.; Morent, R. Plasma Surface Modification of Polylactic Acid to Promote Interaction with Fibroblasts. *J. Mater. Sci. Mater. Med.* **2013**, *24* (2), 469–478. https://doi.org/10.1007/s10856-012-4807-z.

(39) Oyama, T. G.; Kimura, A.; Nagasawa, N.; Oyama, K.; Taguchi, M. Development of Advanced Biodevices Using Quantum Beam Microfabrication Technology. *Quantum Beam Sci.* **2020**, *4* (1). https://doi.org/10.3390/qubs4010014.

(40) Fu, Y.; Wu, G.; Bian, X.; Zeng, J.; Weng, Y. Biodegradation Behavior of Poly(Butylene Adipate-Co-Terephthalate) (PBAT), Poly(Lactic Acid) (PLA), and Their Blend in Freshwater with Sediment. *Molecules* **2020**, *25* (17). https://doi.org/10.3390/molecules25173946.

(41) Poonkottil, N.; Solano, E.; Muriqi, A.; Minjauw, M. M.; Filez, M.; Nolan, M.; Detavernier, C.; Dendooven, J. Spatially Templated Nanolines of Ru and RuO_2 by Sequential Infiltration

Synthesis. *Chem. Mater.* **2022**, *34* (23), 10347–10360. https://doi.org/10.1021/acs.chemmater.2c01866.

(42) Ahlrichs, R.; Bär, M.; Häser, M.; Horn, H.; Kölmel, C. Electronic Structure Calculations on Workstation Computers: The Program System Turbomole. *Chem. Phys. Lett.* **1989**, *162* (3), 165–169. https://doi.org/10.1016/0009-2614(89)85118-8.

(43) Adamo, C.; Barone, V. Toward Reliable Density Functional Methods without Adjustable Parameters: The PBE0 Model. *J. Chem. Phys.* **1999**, *110* (13), 6158–6170. https://doi.org/10.1063/1.478522.

(44) Schäfer, A.; Horn, H.; Ahlrichs, R. Fully Optimized Contracted Gaussian Basis Sets for Atoms Li to Kr. *J. Chem. Phys.* **1992**, *97* (4), 2571–2577. https://doi.org/10.1063/1.463096.

(45) Kresse, G.; Hafner, J. Ab Initio Molecular Dynamics for Liquid Metals. *Phys. Rev. B* **1993**, *47* (1), 558–561. https://doi.org/10.1103/PhysRevB.47.558.

(46) Kresse, G.; Furthmüller, J. Efficiency of Ab-Initio Total Energy Calculations for Metals and Semiconductors Using a Plane-Wave Basis Set. *Comput. Mater. Sci.* **1996**, *6* (1), 15–50. https://doi.org/10.1016/0927-0256(96)00008-0.

(47) Kresse, G.; Furthmüller, J. Efficient Iterative Schemes for Ab Initio Total-Energy Calculations Using a Plane-Wave Basis Set. *Phys. Rev. B* **1996**, *54* (16), 11169–11186. https://doi.org/10.1103/PhysRevB.54.11169.

(48) Perdew, J. P.; Burke, K.; Ernzerhof, M. Generalized Gradient Approximation Made Simple. *Phys. Rev. Lett.* **1996**, *77* (18), 3865–3868. https://doi.org/10.1103/PhysRevLett.77.3865.

(49) Kresse, G.; Joubert, D. From Ultrasoft Pseudopotentials to the Projector Augmented-Wave Method. *Phys. Rev. B* **1999**, *59* (3), 1758–1775. https://doi.org/10.1103/PhysRevB.59.1758.

(50) Grimme, S.; Antony, J.; Ehrlich, S.; Krieg, H. A Consistent and Accurate Ab Initio Parametrization of Density Functional Dispersion Correction (DFT-D) for the 94 Elements H-Pu. *J. Chem. Phys.* **2010**, *132* (15), 154104. https://doi.org/10.1063/1.3382344.

(51) Caligiore, F. E.; Nazzari, D.; Cianci, E.; Sparnacci, K.; Laus, M.; Perego, M.; Seguini, G. Effect of the Density of Reactive Sites in P(S-r-MMA) Film during Al_2O_3 Growth by Sequential Infiltration Synthesis. *Adv. Mater. Interfaces* **2019**, *6* (12), 1900503. https://doi.org/10.1002/admi.201900503.

(52) Frascaroli, J.; Cianci, E.; Spiga, S.; Seguini, G.; Perego, M. Ozone-Based Sequential Infiltration Synthesis of Al $_2$ O $_3$ Nanostructures in Symmetric Block Copolymer. *ACS Appl. Mater. Interfaces* **2016**, *8* (49), 33933–33942. https://doi.org/10.1021/acsami.6b11340.

(53) Dandley, E. C.; Needham, C. D.; Williams, P. S.; Brozena, A. H.; Oldham, C. J.; Parsons, G. N. Temperature-Dependent Reaction between Trimethylaluminum and Poly(Methyl Methacrylate) during Sequential Vapor Infiltration: Experimental and Ab Initio Analysis. *J. Mater. Chem. C* **2014**, *2* (44), 9416–9424. https://doi.org/10.1039/C4TC01293C.

Table of Contents